Applied Energy 217 (2018) 66–74

Contents lists available at ScienceDirect

Applied Energy

journal homepage: www.elsevier.com/locate/apenergy

An electromagnetic rotational energy harvester using sprung eccentric rotor, driven by pseudo-walking motion

M.A. Halim[a,*], R. Rantz[a], Q. Zhang[b], L. Gu[b], K. Yang[b], S. Roundy[a]

[a] Dept. of Mechanical Engineering, University of Utah, Salt Lake City, UT 84112, USA
[b] MEMS Development Group, Analog Devices Inc., Wilmington, MA 01887, USA

HIGHLIGHTS

- An electromagnetic energy harvester using sprung eccentric rotor is proposed.
- System dynamics of the device has been investigated through numerical analysis.
- Model validation is performed by testing a prototype under pseudo-walking motion.
- Harvest higher level of power (6 times) than its conventional counterpart.
- Able to harvest higher power from human wrist motion during walking, running/jogging.

ARTICLE INFO

Keywords:
Electromagnetic energy harvester
Pseudo-walking motion
Eccentric rotor
Torsional spring
Magnet pole-pairs
Mechanical swing-arm

ABSTRACT

In this work, an electromagnetic energy harvesting device using a sprung eccentric rotor has been designed, optimized and characterized to harvest power from pseudo-walking signals (a single frequency sinusoidal signal derived from motion of a driven pendulum that approximates the swing of a human-arm during walking). Our analysis shows that a rotor with an eccentric mass suspended by a torsional spring enhances the mechanical energy captured from low-frequency excitations (e.g., those produced during human walking, running/jogging). An electromagnetic transducer in the sprung eccentric rotor structure converts the captured mechanical energy into electrical energy. An electromechanical dynamic model of a sprung eccentric rotor has been developed and an optimization routine was performed to maximize output power under pseudo-walking excitation. The structure of the electromagnetic transducer was refined using Finite Element Analysis (FEA) simulations. A prototype energy harvester was fabricated and tested in a pseudo wrist-worn situation (by mounting on a mechanical swing-arm) to mimic the low-frequency excitation produced during human walking. A series of pseudo-walking motions was created by varying the swing profile (angle and frequency). The prototype with optimal spring stiffness generates a maximum 61.3 μW average power at $\pm 25^{\circ}$ rotational amplitude and 1 Hz frequency which is about 6-times higher than its unsprung counterpart under same excitation condition. The experimental results are in good agreement with the simulation results.

1. Introduction

Modern portable and wearable consumer electronic devices (e.g., smart watches, body sensors, activity trackers, smart training shoes, etc.) contain a number of fully-embedded wireless sensors with multi-functional and low-power consuming features [1]. However, these low-power sensors still require external power, and are generally powered by conventional electrochemical batteries (e.g., Li-ion, Li-Po, fuel cells, etc.). Electrochemical batteries have a limited lifetime and require periodic charging or replacement which is often inconvenient, or even impossible in remote locations and contingent situations [2]. Moreover, since most of the batteries contain toxic metals (such as cadmium, mercury, lead, lithium, or manganese), disposal of the expired batteries and cells produces hazardous waste that exacerbates environmental pollution and poses threats to both human and animal health. Therefore, there is great interest in developing self-powered electronics for sustainable and long-lasting operation by eliminating the need for recharging or replacing their external power sources. Energy harvesting from ambient/environmental energy sources (e.g., light, heat, sound, vibration, etc.) is considered one solution to address these circumstances [3–5]. Mechanical vibration, in the form of kinetic energy, is one of the most available ambient/environmental energy sources in

* Corresponding author.
E-mail address: halim.miah@utah.edu (M.A. Halim).

https://doi.org/10.1016/j.apenergy.2018.02.093
Received 17 October 2017; Received in revised form 10 February 2018; Accepted 12 February 2018
Available online 27 February 2018

machinery operations, civil infrastructures, air-ground transportations, as well as human-body-induced motion which can be converted into electrical energy by employing compatible electromechanical transduction systems [6]. Commonly used electromechanical transduction mechanisms include piezoelectric [7,8], electromagnetic [9,10], electrostatic [11,12], magnetostrictive/magnetoelectric [13,14], and triboelectric [15,16] mechanisms.

The performance of a vibration energy harvester greatly depends on the characteristics of the vibration source, type of transduction mechanism used and how the transducer is coupled to the mechanical system. Generally, vibration energy harvesters utilize inertial mechanism for electromechanical coupling. A proof-mass, mounted in a reference frame attached to the vibrating body, couples the kinetic energy (while the body is in motion) to a transducer (piezoelectric, electromagnetic, or other) that generates electrical power. Depending on the source of vibration, some harvesters have been developed as resonant [17–19], others as wideband [20–22]. Among different sources, vibration produced by the motion of the human-body during daily activities (e.g., walking, running/jogging, performing an office task, etc.) exhibits low-frequency, large-amplitude, and random characteristics [23,24]. In order to capture energy from such low-frequency, large-amplitude motion of the human-body, clever design approaches are required. Numerous design approaches including a non-linear spring, mechanical/magnetic plucking, and mechanical impact have been proposed over the past few years. Saha et al. [25] developed a nonlinear magnetic spring based electromagnetic generator for human body motion during walking and slow running. Liu et al. [26] investigated a similar nonlinear electromagnetic energy harvester for hand-shaking vibration. Wei et al. [27] demonstrated a mechanically plucked piezoelectric energy harvester from human walking motion for different speeds. Halim et al. [28] presented a miniaturized electromagnetic energy harvester for human-body-induced motion using an impact-driven frequency up-conversion technique. And, Geisler et al. [29] reported a 1D inertial electromagnetic energy harvester using a free-moving magnet stack between two repulsive magnets. All of these inertial devices use linear inertial-mass motion. However, the power output of such linear energy harvesters can be limited by the internal travel range of its inertial-mass motion, especially for low-frequency excitations (e.g., human-body-induced vibration). To overcome this limitation of linear motion based harvesters, devices with rotational inertial mass have been adopted by researchers that utilize an eccentric rotor structure to couple the kinetic energy into the transducer element. Romero et al. [30] presented a micro-rotational electromagnetic energy harvester for extracting energy from human motion at joint locations. Pillatsch et al. [31] introduced a rotational piezoelectric energy harvester for human upper arm motion during walking/running using magnetic plucking principle, Nakano et al. [32] reported the development of an electret-based microelectromechanical system (MEMS) rotational energy harvester by patterning fan-shaped electrets and guard electrodes on an eccentric rotor, and interdigitated electrodes on the stator for capturing the kinetic energy of human-motion. Lockhart et al. [33] presented a compact, wearable piezoelectric on-body harvesting system using a small eccentric mass to mechanically deflect a set of micromachined piezoelectric cantilevers when excited by the low frequency movements of the human-body. However, the proof-mass rotational amplitude of such eccentric rotor structures is quite small during walking; a larger rotational amplitude results in higher power output. Effective design of the rotational unit enhances the rotational amplitude, which, in turns, increases the output power. Yeatman [34] mathematically analyzed the maximum achievable power of both non-resonant oscillating and resonant oscillating rotational devices by using a planar rotor model which accounted for rotational and linear excitations separately. However, the mathematical analysis was not further explored either via simulation or by experiment. Due to complex nature of human-body-induced motion, a multidimensional model is required to estimate the maximum possible power generation from such rotational energy harvesting devices. We have extended the rotational model presented in [34] to three dimensions and have included linear and rotational excitations together (including the effect of gravity) [35]. Recently, we have presented an improved (sprung) eccentric rotor architecture (by the extended three dimensional model) to evaluate (via simulation) the maximum power output using real walking data from a number of subjects as inputs [36]. It reported that the estimated power outputs were different for different subjects because of the unique walking pattern (e.g., swing frequency and amplitude, bias angle, etc.) of each subject. Moreover, in a real-world situation (test on human subject while walking/running), the same result may not be reproduced (on the same subject) due to variation in the motion from one run to another. Therefore, an extensive analysis and a robust validation is required for fair evaluation of the proposed rotational energy harvesting structure.

In this work, we have presented an electromagnetic rotational energy harvester using an improved (sprung) eccentric rotor structure to harvest kinetic energy from a pseudo-walking signal generated by a human-arm-like mechanical swing-arm. An electromechanical dynamic model has been developed and optimized. Both numerical and finite element method (FEM) simulations have been performed to predict the performance of the proposed electromechanical structure. Finally, a prototype device has been fabricated and characterized on the bench-top test setup under a series of pseudo-walking excitation inputs. Results show that under optimal conditions (electrical damping, torsional spring stiffness, etc.), a harvester with a sprung eccentric rotor enhances the mechanical energy capture and outperforms its unsprung counterpart. Following the introduction, Section 2 will discuss the design of the sprung eccentric rotor structure and the development of an electromagnetic energy harvester using the sprung eccentric rotor, from which the prototype system architecture will be developed. The dynamic behavior and system performance will be investigated in Section 3. The fabrication of a prototype and the measurement of its damping characteristics will be discussed in Section 4. Subsequently, the performance of the fabricated prototype will be verified by carrying out a series of pseudo-walking tests in Section 5. Finally, Section 6 concludes the article.

2. Architecture of the proposed energy harvesting system

2.1. Sprung eccentric rotor design

Our design procedure starts with the development and analysis of a generalized three-dimensional model of an energy harvester comprised of an eccentric seismic mass and a torsional spring that couples the seismic mass to the reference frame and allows it to rotate about an axis on a low-friction bearing, as shown in Fig. 1. Note that the torsional spring holds the seismic mass vertically upwards at $\pi/2$ radians when subject to no external force. It includes both mechanical and electrical dampers, representing energy losses due to friction and energy extraction from an ideal energy transducer, respectively. Although the rotational or linear excitation inputs work on the system in three-dimensions, the rotation of the sprung eccentric rotor is constrained to motion in the X-Y plane. Therefore, the governing equation of the rotor motion in the X-Y plane is [37].

$$(ml^2 + I_G)(\ddot{\theta}_z + \ddot{\phi}_z) + (C_m + C_e)\dot{\phi}_z + K_{sp}\left(\phi_z - \frac{\pi}{2}\right) = ml(\ddot{X}sin\phi_z - \ddot{Y}cos\phi_z) \tag{1}$$

where m, l, and I_G are the eccentric mass, eccentric length and moment of inertia of the rotor about the center of gravity, respectively. $\ddot{X}$ and $\ddot{Y}$ are the input accelerations to the system working along X and Y coordinates, respectively. C_m and C_e are the mechanical and electrical damping coefficients, respectively. K_{sp} is the stiffness of the torsional spring. θ_z is the rotational input to the reference frame along Z direction and ϕ_z is the angular displacement of the rotor relative to the reference

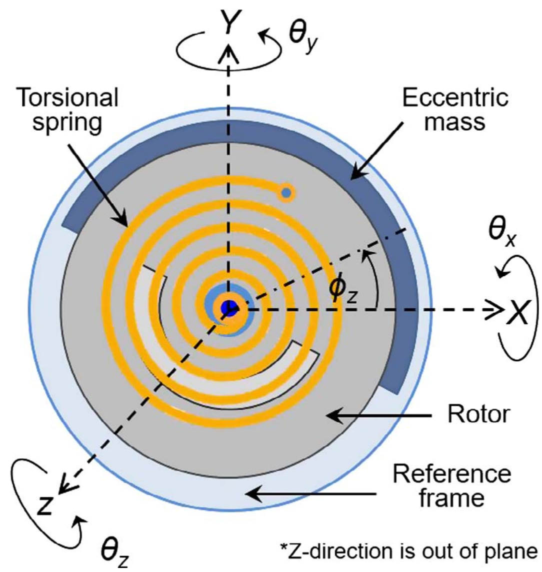

Fig. 1. Schematic representation of a sprung eccentric rotor: θ_x, θ_y and θ_z are the rotational inputs whereas X, Y, and Z are the linear inputs to the reference frame.

frame. It is to be noted that the input accelerations are a combination of linear acceleration due to motion and gravitational acceleration.

2.2. Harvester structure and its operation

To convert the mechanical energy absorbed by the sprung eccentric rotor into electrical energy, an electromagnetic transducer has been incorporated within the rotor. Fig. 2 shows the schematic structure of the proposed electromagnetic energy harvester (EMEH) using a sprung eccentric rotor.

It consists of a dual eccentric rotor (two sides rotate together) with a torsional spring, containing five NdFeB (N52) magnet pole-pairs with a back-iron shield (in each rotor) and ten self-supported copper coils (series connected) placed in the middle of the dual-rotor structure using a PCB (fixed to the housing) interconnect. The back-iron shields on either side of the dual-rotor increase the magnetic flux densities in the middle where the coils are placed. Upon excitation, relative motion between the magnet pole-pairs and the coils occurs which, in turn, induces an electromotive force (e.m.f.), according to Faraday's law of electromagnetic induction, as

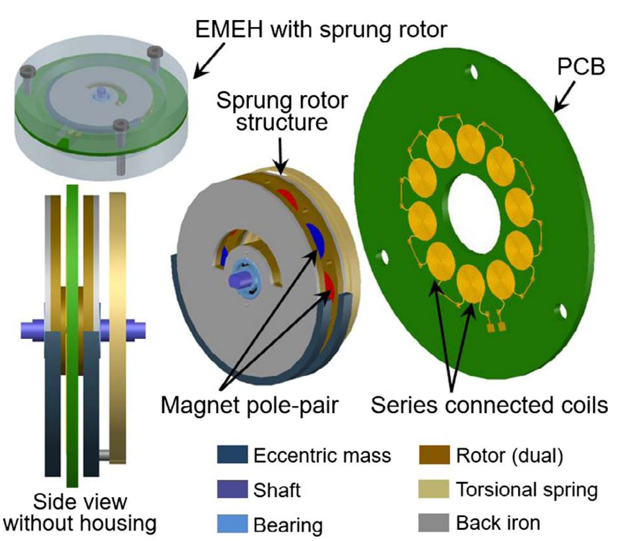

Fig. 2. Schematic structure of the proposed electromagnetic energy harvester using sprung eccentric rotor.

$$V_{em}(t) = N\frac{d\Phi_B}{dt} = N\frac{d\Phi_B}{d\phi_z}\dot{\phi}_z \tag{2}$$

where N is the total number of the coil turns, Φ_B is the net magnetic flux captured by all coils and $\dot{\phi}_z$ is the relative angular velocity between the magnet pole-pairs (in other words, the rotor) and the coils that will be determined by numerically solving the governing equation of the rotor motion, presented in (1). With a resistive load R_l (equal to the coil resistance R_c) connected to the coil terminals, the power delivered to R_l (coil inductance is neglected since its impedance is significantly smaller at signal frequencies below 1 kHz) is

$$P(t) = \frac{V_{em}(t)^2}{4R_l} = \frac{1}{2}\left[\left(N\frac{d\Phi_B}{d\phi_z}\right)^2\frac{1}{2R_l}\right]\dot{\phi}_z^2 \tag{3}$$

And the maximum average power is

$$P_{avg} = \frac{1}{T}\int_0^T P(t)dt \tag{4}$$

where the term in the square brackets in (3) represents the electrical damping coefficient C_e of the electromechanical system. We have determined the electrical damping coefficient C_e, the mechanical damping coefficient C_m and spring stiffness K_{sp} experimentally by observing and analyzing the decay envelope of angular motion during free oscillation of the eccentric rotor after deflecting it by 90° from its stable equilibrium position (This will be discussed in Section 4).

3. Performance prediction by simulation

3.1. Finite element analysis

The rate of change of magnetic flux ($d\Phi_B/d\phi_z$) has been determined by Finite Element Analysis (FEA) simulation using COMSOL Multiphysics. Fig. 3 shows the schematic of a single magnet pole-pair. θ_p (left) is the pole pair angle. A cross-section of two aligned magnet pole-pairs with a coil is shown on the right. A single pole pair was used in the FEA simulation to determine the rate of change of magnetic flux with respect to the relative angular displacement of the pole-pairs within the coil. The pole-pair angle θ_p refers to the angular distribution of one permanent magnet pole-pair as $\theta_p = 360°/p$, where p is the number of pole-pairs.

3.2. Numerical simulation

To predict the electromechanical behavior of the proposed design and investigate the energy harvesting performance under various pseudo-walking scenarios (variable frequencies and excitation amplitudes), the mathematical model (Eq. (1)) has been solved numerically using MATLAB. The simulation parameters include rotating mass, inertia about the center of gravity, eccentric length of the eccentric rotor (determined using SolidWorks computer aided design software's mass

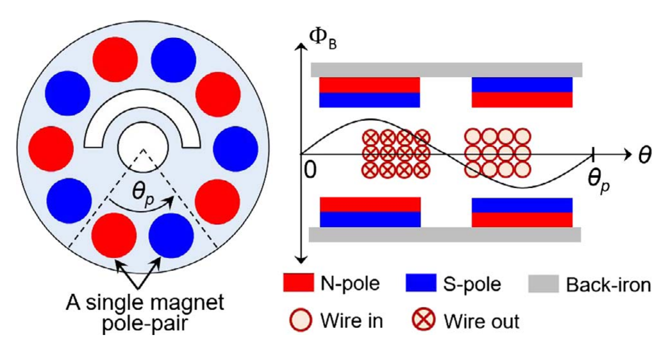

Fig. 3. Schematic of a single magnet pole-pair incorporated in the rotor (left) and the cross-section of two aligned magnet pole-pairs with a coil (right) used in the FEA simulation.

Table 1
Simulation parameters of the proposed EMEH using sprung eccentric rotor.

Parameter	Value
Mass of the eccentric rotor	10.7×10^{-3} kg
Inertia about center of gravity	8.2×10^{-7} kg m^2
Eccentric length of the rotor	1.52×10^{-3} m
Mechanical damping coefficient	0.6×10^{-6} N m s/rad
Electrical damping coefficient	1.9×10^{-6} N m s/rad
Stiffness of the torsional spring	$0 \sim 3.0 \times 10^{-4}$ N m/rad
Excitation frequency	0.91 Hz
Excitation amplitudes	$\pm 12.5^\circ$, $\pm 18^\circ$ and $\pm 25^\circ$
Load resistance (optimum value)	240 Ω

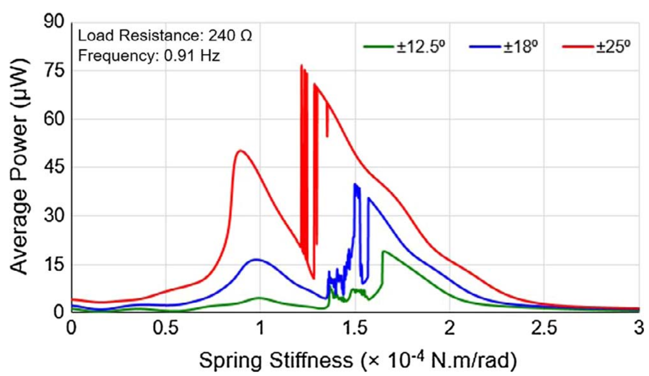

Fig. 4. Numerical simulation of the average power output vs. torsional spring stiffness under different pseudo-walking input excitations at 0.91 Hz.

properties tool), various spring stiffnesses and average values of mechanical and electrical damping coefficients (determined experimentally) as shown in Table 1. As the eccentric rotor travels through the gravity field (under the excitation of the arm swing), the appropriate projections of the gravity vector have been accounted for in the numerical simulation, in addition to the other (linear) accelerations that are a result of the pendulum kinematics. In the simulation, it is observed that under certain pseudo-walking input excitations, the dynamic response of the eccentric rotor is greatly influenced by the stiffness of the torsional spring which, in turn, affects the power and voltage generation of the system. Fig. 4 shows the numerical simulation of the average power (delivered to a matched load) as a function of torsional spring stiffness for different rotational amplitudes at 0.91 Hz pseudo-walking frequency. Note that all of the results were obtained under steady-state conditions in order to eliminate the effect of transients. It is observed that the sprung eccentric rotor device exhibits highly nonlinear behavior resulting in two major peaks in power output. The dense area (between the two stable peaks) in each plot contains a number of unstable peaks suggesting the existence of two stable solution branches: a set of large oscillation magnitude solutions and a set of small oscillation magnitude solutions. In the numerical simulation output, the power appears to jump between these two solutions. The stiffness value at which the highest output power is obtained has been considered to be the optimal spring stiffness value which is 1.3×10^{-4} N m/rad for $\pm 25^\circ$. However, for small swing angles ($\pm 18^\circ$ and $\pm 12.5^\circ$), the sprung device does not perform best for spring stiffness of 1.3×10^{-4} N m/rad. It performs best with the spring stiffnesses of 1.5×10^{-4} N m/rad and 1.66×10^{-4} N m/rad for $\pm 18^\circ$ and $\pm 12.5^\circ$, respectively. The optimal spring stiffness is different for different swing angles due to the highly nonlinear effect of the system which also limits its validity within a certain frequency range (see Fig. 12).

We also performed time-domain numerical simulations to predict the non-linear displacement behavior of the eccentric rotor and output voltage generated by the rotational energy harvesters (without and with torsional spring). Fig. 5 shows the angular displacement

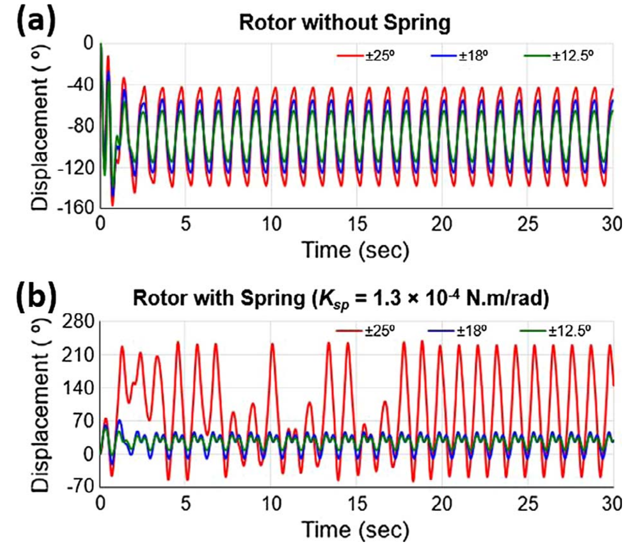

Fig. 5. Numerical simulation of non-linear displacement waveforms of the eccentric rotor (a) without spring and (b) with spring under different pseudo-walking input excitations at 0.91 Hz frequency (with 240 Ω optimum load resistance).

waveforms of the eccentric rotors (both unsprung and sprung of $K_{sp} = 1.3 \times 10^{-4}$ N m/rad) under different rotational amplitudes at 0.91 Hz pseudo-walking frequency. Note that the unsprung eccentric rotor oscillates about a point which is π radians off from the sprung device because the torsional spring tends to hold the eccentric mass vertically upward at $\pi/2$ radians. The results presented in Fig. 4 may be better understood in light of the waveforms presented in Fig. 5b. The two peaks in Fig. 4 correspond to two different modes of oscillation that the harvester exhibits depending on the nature of the excitation and the degree of spring stiffness. The first, lower amplitude peak corresponds to oscillations in which the rotor remains on a single side (from its stable equilibrium position at $\pi/2$ radians) of the device, generally producing lower power relative to the second peak. See Fig. 5b for examples of this kind of trajectory for input excitation amplitudes of $\pm 18^\circ$ and $\pm 12.5^\circ$. The second, larger amplitude peak corresponds to a trajectory whereby the rotor oscillates between both sides of the device about the $\pi/2$ position, generally producing more power than in the single-sided trajectory case. See Fig. 5b for an example of this kind of trajectory for the input excitation amplitude of $\pm 25^\circ$.

The predicted output voltage waveforms across an optimal load, for both unsprung and sprung (1.3×10^{-4} N m/rad) devices under same excitation conditions are presented in Fig. 6. Results show that the output voltage waveforms generated by the unsprung device for all swing angles and those generated by the sprung device for smaller swing angles ($\pm 18^\circ$ and $\pm 12.5^\circ$) are stable. However, the voltage waveform generated by the sprung device for a $\pm 25^\circ$ swing angle is unstable. The stiffness (1.3×10^{-4} N m/rad) of the sprung rotor is very close to the dense zone of the graph in Fig. 4, thus it possibly enters into the regime of spring stiffness that may produce chaotic voltage waveforms. The root mean square (rms) values of the voltages generated by the sprung device (in all three cases) are higher than those generated by the unsprung device. Note that in calculating the rms values, data from the first three seconds was discarded in an effort to minimize the effects of initial conditions.

4. Prototype and its damping characteristics

4.1. Prototype fabrication

In order to validate the model prediction, an EMEH prototype was fabricated and tested. Fig. 7(a) shows the components of the energy harvester. It has a dual eccentric rotor. Each rotor is composed of a

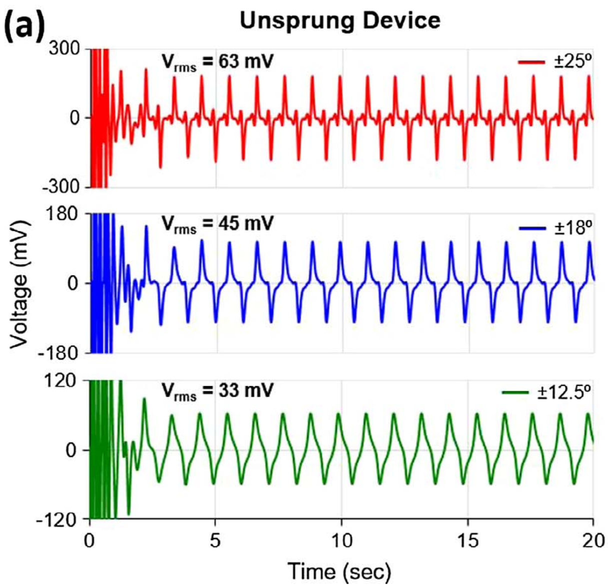

Fig. 6. Numerical simulation of the voltage waveforms across optimum load resistance generated by the (a) unsprung and (b) sprung devices under different pseudo-walking input excitations at 0.91 Hz frequency (with 240 Ω optimum load resistance).

brass magnet-carriage containing five magnet pole-pairs (N52 NdFeB), a back-iron shield (made of 1008–1010 steel) behind the magnet pole-pairs of the rotor and a half-annulus shaped tungsten mass glued to the side of the rotor. Both the rotors were aligned together so that they work as a single eccentric rotor that rotates about the shaft with the help of two high precision stainless steel ball bearings. Ten self-supported coils (using 44 AWG laminated copper wire) were wound and connected in series with the help of a custom PCB interconnect that works as the coil carriage. Note that the adjacent coils were placed in alternating wound/anti-mound orientations since the adjacent magnets (the pole-pair) placed in the rotor have opposite polarity. The PCB coil carriage was placed in the middle of the dual rotor and was fixed to the aluminum harvester body. A phosphor bronze torsional spring was installed underneath the bottom rotor by attaching its inner edge to the shaft (using a spring collar attached to the shaft) and the outer edge to the rotor (with the help of a cylindrical shaped metal post). Fig. 7(b) shows a fully assembled prototype energy harvester of volume

Table 2
Geometric parameters of the proposed EMEH prototype.

Parameter	Value
Magnet dimension	Ø4.8 mm × 0.8 mm
Rotor (each) dimension with tungsten	Ø25.2 mm × 0.8 mm
Back-iron thickness	0.5 mm
Tungsten thickness	1.3 mm
Coil inner diameter	1.2 mm
Coil outer diameter	4.8 mm
Coil height	0.8 mm
No. of coil turns (each)	300
Coil resistance (each)	24 Ω
PCB thickness	0.8 mm
Air-gap between magnet and coil	0.6 mm
Functional unit dimension	Ø25.2 mm × 7 mm
Overall prototype dimension	Ø40 mm × 16 mm
Weight of the prototype (with spring)	42 g

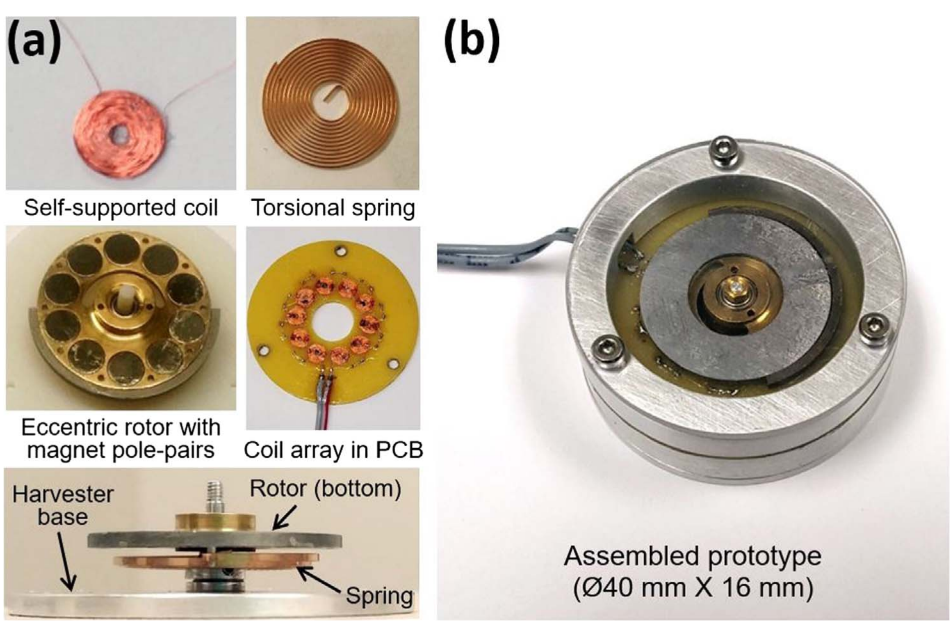

Fig. 7. Photographs of the (a) harvester components and (b) fully assembled prototype.

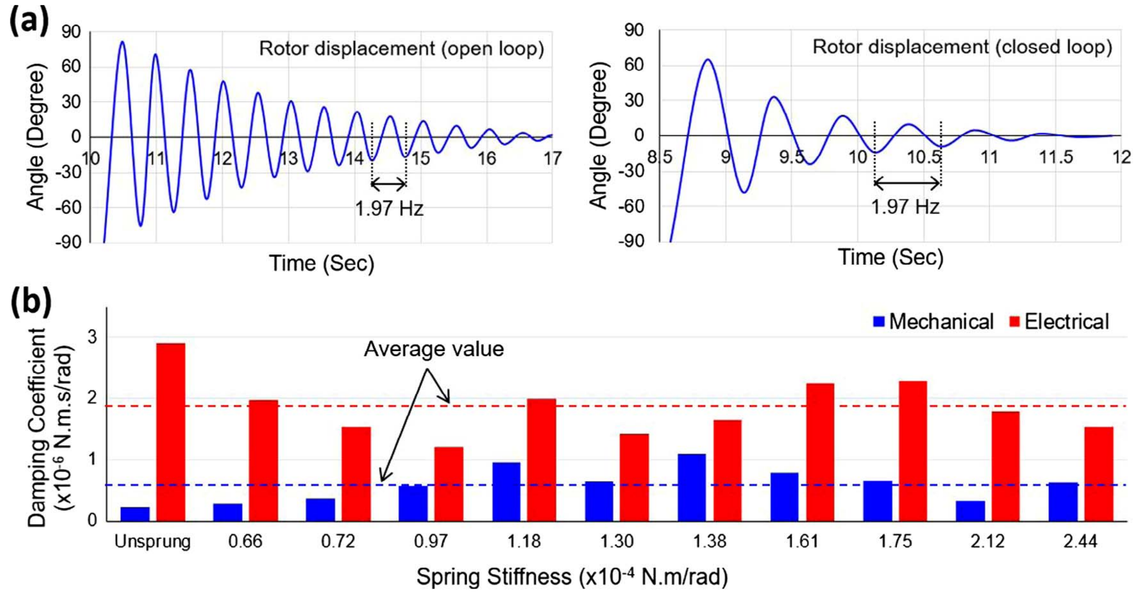

Fig. 8. (a) Exponentially decayed angular displacement waveforms (open loop and closed loop) of the eccentric rotor when released from a 90° starting position and (b) variation of damping coefficients (both mechanical and electrical) with the torsional spring stiffness.

$\sim 20\,cm^3$. However, the functional volume (volume without housing) of the prototype is $\sim 3.5\,cm^3$. As we needed to assemble and dissemble the prototype many times to change/remove the spring, to measure the damping characteristics, and to test the device with springs of various stiffnesses, we made an oversized housing for ease of handling during those operations. However, a more portable design and standard packaging materials can be used to reduce the overall volume of the fully assembled device. The geometric parameters of the prototype are given in Table 2.

4.2. Damping characteristics for various spring stiffness

The damping (both mechanical and electrical) characteristics for various spring stiffness were determined by analyzing the free oscillation of the eccentric rotor after deflecting it (by 90°) from its stable equilibrium position. Using a high speed camera, we recorded the angular displacement of the eccentric rotor for both open loop and closed loop (with 240 Ω optimum load resistance) conditions. The displacements, determined using video editing software, were reproduced as shown in Fig. 8(a). Then, the damping coefficients (C_m for open loop and C_e for closed loop) were calculated using the logarithmic decrement method with the following set of equations

$$\text{Logarithmic decrement,}\delta = \frac{1}{n}ln\frac{x(t)}{x(t+nT)} \tag{5}$$

$$\text{Damping ratio,}\zeta = \frac{1}{\sqrt{1+\left(\frac{2\pi}{\delta}\right)^2}} \tag{6}$$

$$\text{Damping coefficient,}C = 2\zeta J\omega_n\sqrt{1-\zeta^2} \tag{7}$$

where $x(t)$ is the amplitude at time t and $x(t+nT)$ is the amplitude of the peak n periods away, where n is any integer number of successive positive peaks. J and ω_n ($2\pi f_n$) are the inertia about center of rotation and the angular natural frequency of the eccentric rotor, respectively. The spring stiffness was calculated by using $K_{sp} = J\omega_n^2$. This process was repeated for the sprung eccentric rotor with various spring stiffnesses, as well as the unsprung eccentric rotor which was allowed to oscillate under the effect of gravity. Fig. 8(b) shows the variation of both mechanical and electrical damping coefficients with the rotational spring stiffness. Note that the unsprung eccentric rotor has zero spring stiffness. Every component of the prototype was disassembled while changing the spring with corresponding spring stiffness and then reassembled before collecting the video data.

The assembly issues (installing the spring, putting the rotor back to the shaft by sliding the ball bearing, etc.) might cause some test to test variation in the damping values. However, the average values were used in the numerical analysis.

The values of measured natural frequencies (frequencies of free oscillation by deflecting from stable equilibrium position) of the unsprung eccentric rotor and sprung eccentric rotor of various spring stiffnesses are very much different from the pseudo-walking excitation frequencies (0.8 Hz – 1.25 Hz). For unsprung eccentric rotor, the natural frequency is 2.35 Hz and the mechanical Q-factor ($Q_m = 1/2\zeta_m$) is calculated as 55. For sprung eccentric rotor, the natural frequencies range from 1.41 Hz to 2.70 Hz for various spring stiffness values ranging from 0.66×10^{-4} N m/rad to 2.44×10^{-4} N m/rad and the corresponding mechanical Q-factor values range between 10 and 26.

5. Experimental results and discussion

5.1. Pseudo-walking test setup

In order to characterize the EMEH under pseudo-walking excitation, the prototype energy harvester was tested in a pseudo wrist-worn situation by mounting it on a mechanical swing-arm in order to provide a controlled pseudo-walking excitation. It is comprised of a microprocessor-controlled stepper motor, driving a half-meter long (determined based on the length of a human-arm, from shoulder to wrist) aluminum pendulum with sinusoidal angle. The prototype is mounted on the distal end of the pendulum. A series of pseudo-walking excitations was created by varying the swing profiles (angle and frequency). The output voltages generated by the prototype under various input excitations were observed and recorded for further analysis by an oscilloscope (Picoscope 4824: Pico Technology, UK). Fig. 9(a) shows the schematic of the pseudo-walking test setup whereas Fig. 9(b) shows its photograph.

5.2. Test results

Testing started with the measurement of optimum load resistance to get the maximum average power generated by the harvester prototype for different pseudo-walking input excitations. The output terminals of

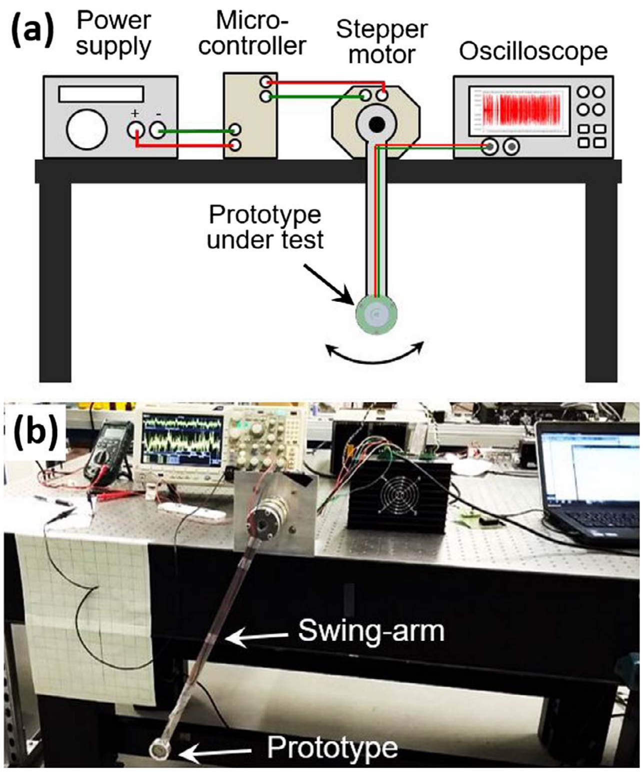

Fig. 9. (a) Schematic of the pseudo-walking test setup and (b) a photograph of the experiment while the prototype was mounted on the mechanical swing-arm.

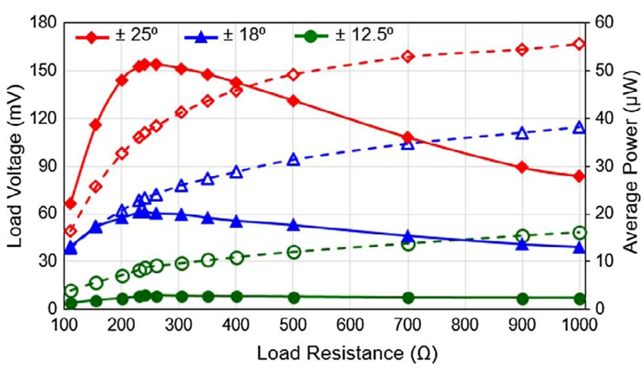

Fig. 10. Variation of the RMS voltage (dotted lines) and average power (solid lines) with load resistance to determine the optimum load resistance for the sprung device.

the prototype were connected to continually adjustable load resistors and the resistance values were swept in a range from 100 Ω to 1 kΩ. Fig. 10 shows the load voltages and average powers as a function of load resistances for the sprung device with optimum spring stiffness (K_{sp} = 1.3 × 10^{-4} N m/rad) under different rotational amplitudes at 0.91 Hz pseudo-walking frequency. Results show that the voltage across the load increases as the value of load resistance increases; however, maximum power is delivered to a 240 Ω load (which is also the case for the device without a spring). Generated power, P_{avg}, is experimentally equal to V_l^2/R_l, where V_l is the RMS voltage across the load R_l. Therefore, all our pseudo-walking tests use 240 Ω optimum load resistance connected to the output terminals of the test devices (both unsprung and sprung).

In order to validate the simulation results and to determine the optimal spring stiffness of the sprung device, we ran the pseudo-walking bench-top tests under different rotational amplitudes at 0.91 Hz pseudo-walking frequency for a range of spring stiffnesses. Fig. 11(a) presents the average generated power as a function of the stiffness of the torsional spring installed in the prototype. Note that the power generation for the unsprung device, shown as the left-most set of generated power data in Fig. 11(a), is not a function of spring stiffness as there is no spring, and thus results in only one set of power data. Results indicate that the performance of the sprung device with a spring stiffness of 1.3 × 10^{-4} N m/rad is the best (51.55 μW) for ± 25° swing angle. For ± 18° swing angle, 1.3 × 10^{-4} N m/rad also gives the best output power (20.6 μW). However, the second best power value (18 μW), obtained for the stiffness value of 1.75 × 10^{-4} N m/rad, is somewhat higher than the 1.5 × 10^{-4} N m/rad predicted by simulation. For ± 12.5° swing angle, the device with 1.75 × 10^{-4} N m/rad spring stiffness gives the highest power output (4.6 μW) whereas it generates second best power (2.9 μW) when the spring stiffness is 1.3 × 10^{-4} N m/rad. Since the sprung device with a spring stiffness of 1.3 × 10^{-4} N m/rad produces the highest power outputs for ± 25° and ± 18° swing angles, we have considered 1.3 × 10^{-4} N m/rad as the optimal spring stiffness. It is to be noted that experimentally validating the exact simulated power output peaks for the corresponding spring stiffness was challenging since only a finite number of of-the-shelf torsional springs could be tested.

It is clear from Fig. 11(a) that the sprung device (with optimal spring stiffness) outperforms the unsprung device. The spring allows the eccentric rotor to respond to a particular excitation profile (rotational amplitude and frequency) with increased velocity resulting in increased voltage and power generation. Fig. 11(b) shows the comparison of load voltage waveforms generated by the unsprung device and the sprung device (with 1.3 × 10^{-4} N m/rad optimal spring stiffness) under different excitation amplitudes at 0.91 Hz pseudo-walking frequency. It is seen from the waveforms that in all cases the peak-peak voltages of the sprung device are higher than those of the unsprung device. Note that the voltage waveform for the unsprung device hovers around zero much of the time. Thus, the RMS voltage improvement (and average power) from the sprung device is larger than the peak-to-peak voltage improvement. When compared to the simulation, a slight difference is observed. This may be due to imperfect assembly of the harvester components (e.g., installing torsional spring, magnet-coil gap, etc.). Also, the coils were wound manually and thus differ from the ideal coils simulated in COMSOL. Additionally, the numerical calculations model only viscous friction, not Coulomb friction. This simplification could have significant effects on the dynamical behavior of the eccentric rotor.

It is obvious that the swing profile (rotational amplitude and frequency) of human-arm motion during vigorous walking/running is different for different human subjects. Therefore, the amount of generated power of a wrist-worn harvester (during walking/running) may vary subject-to-subject. Considering this assumption, in addition to our current pseudo-walking excitation profile (± 25°, ± 18° and ± 12.5° amplitudes at 0.91 Hz frequency), we have also tested our prototype energy harvester under different pseudo-walking frequencies. Fig. 12 shows the measured average power from both unsprung device and sprung device with three representative springs (spring stiffnesses values: 0.97 × 10^{-4} N m/rad, 1.3 × 10^{-4} N m/rad and 1.75 × 10^{-4} N m/rad) under various excitation frequencies and rotational amplitudes of the mechanical swing-arm.

Note that the frequency range of pseudo-walking motion of the swing-arm was chosen from 0.8 Hz to 1.25 Hz because the arm motion frequencies during walking/running for different human subjects lie in this range [23]. Moreover, the rotation response of the eccentric rotor (especially, the unsprung rotor) below 0.8 Hz was too poor to generate significant voltage/power. It is observed from Fig. 12 that the average power generated by the unsprung device increases with increasing pseudo-walking frequency. The maximum power (42.6 μW) is obtained at a swing profile of ± 25° amplitude and 1.25 Hz frequency. On the other hand, the sprung device shows resonant-like behavior for 0.97 × 10^{-4} N m/rad, 1.3 × 10^{-4} N m/rad spring stiffnesses and generates maximum power at 1 Hz pseudo-walking frequency. It generates

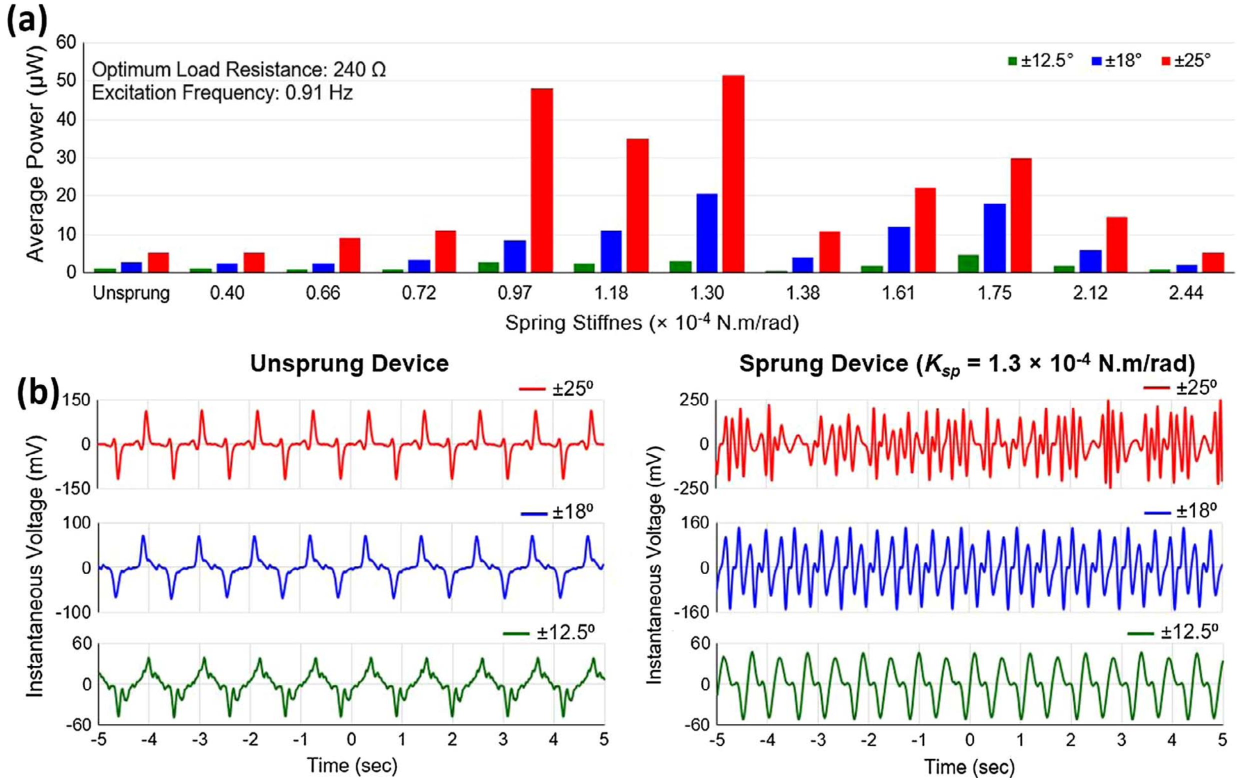

Fig. 11. (a) Measured output power as a function of torsional spring stiffness and (b) generated instantaneous voltage waveforms (across 240 Ω optimum load resistance and at 0.91 Hz excitation frequency) of the unsprung and the sprung devices.

a maximum 61.3 μW average power under ± 25° rotational amplitude and 1 Hz frequency (representative of 3.5 mph walking speed) which is about 6 times higher than the average power (10.4 μW) generated by its unsprung counterpart under the same pseudo-walking excitation profile. For 1.75×10^{-4} N m/rad spring stiffness, power generation increases with the increase in the swing-arm excitation frequency. In this case, the sprung eccentric rotor oscillates on both sides about its steady position (vertically upwards at π/2 radians when subject to no external force) while excited and its rotational velocity increases with the increase in the pseudo-walking frequency which, in turn, increases power output.

It is to be noted that the eccentric rotor (without spring) oscillates freely under the effect of gravity, as a simple pendulum. Installing a torsional spring to the eccentric rotor changes the system dynamics, from that of a simple pendulum (itself a non-linear system with complex dynamics) to an even more complex non-linear rotational spring-mass-damper system. Our study, via simulation and experiment, reveals that use of a spring with optimal or near-optimal spring stiffness significantly improves the performance of the same electro-mechanical transducer.

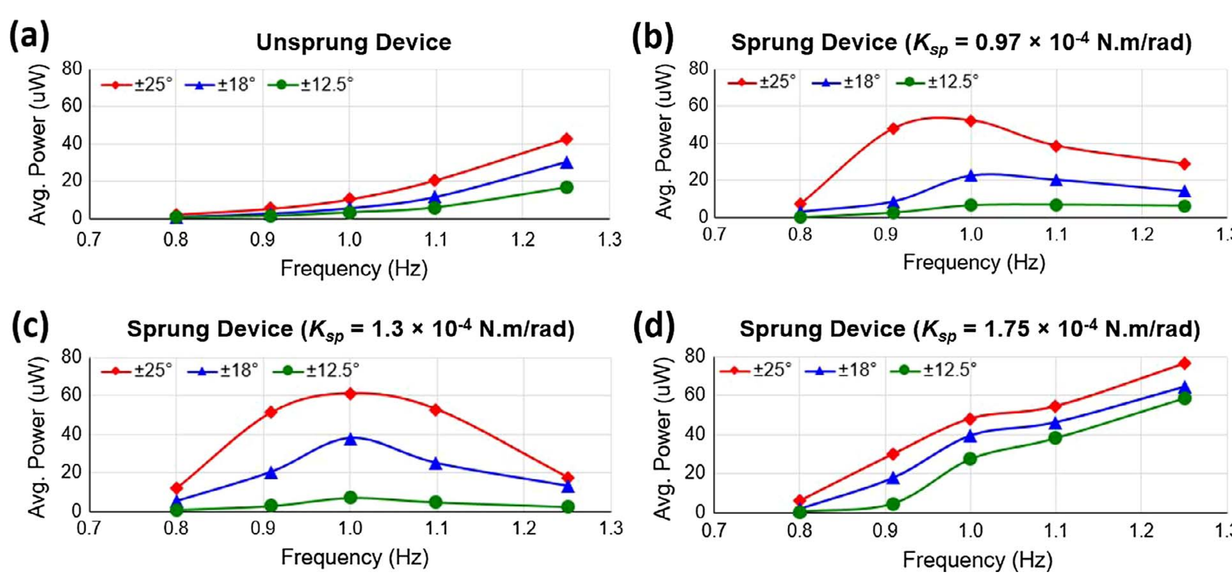

Fig. 12. Measured output power from both unsprung device and sprung device with three representative springs under various excitation frequencies and rotational amplitudes of the mechanical swing-arm.

6. Conclusions

The reported work demonstrated the potential of a sprung eccentric rotor structure to harvest power using an electromagnetic transducer from pseudo-walking excitation that mimics the swing motion of a human-arm during walking/running. An electromechanical model of the proposed system was developed with which numerical simulations were performed to predict its power generation capability under various pseudo-walking excitation scenarios. The simulation results were verified by building a prototype and testing it in a pseudo wrist-worn situation. Test results showed good agreement with the simulation results. The performance of the sprung device (with optimal or near-optimal spring stiffness) is very promising compared to its unsprung counterpart. The power output of the sprung device, with optimum spring stiffness, 1 Hz frequency and $\pm 25^{\circ}$ rotational amplitude, is about 6 times higher than the power generated by the unsprung one under the same excitation conditions. Results indicate that a sprung rotational electromechanical transducer effectively couples the extremely low-frequency motion (generated during human-like-arm swing) and improves the energy harvesting performance significantly. Future work will include further evaluation of the complex nature of the human-arm swing characteristics (for various daily activities in various situations), optimizing the harvester accordingly and testing an optimized prototype in a real-world situation by mounting it on the wrists of a number of human subjects and collecting the output results during daily activities (e.g., walking, running/jogging, office tasks, etc.).

Acknowledgments

Funding for this research was provided by the National Science Foundation under Award Number ECCS 1342070, and a generous grant from Analog Devices Inc.

References

[1] Sodano HA, Inman DJ, Park G. A review of power harvesting from vibration using piezoelectric materials. Shock Vib Dig 2004;36:197–205.
[2] Anton SR, Sodano HA. A review of power harvesting using piezoelectric materials (2003–2006). Smart Mater Struct 2007;16:R1–21.
[3] Cook-Chennault KA, Thambi N, Sastry A. Powering MEMS portable devices- a review of non-regenerative and regenerative power supply system with special emphasis on piezoelectric energy harvesting systems. Smart Mater Struct 2008;17:043001.
[4] Priya S, Inman DJ. Energy harvesting technologies. 1st ed. New York: Springer; 2009.
[5] Briand D, Yeatman E, Roundy S. Micro energy harvesting. 1st ed. Germany: Wiley-VCH; 2015.
[6] Beeby SP, Tudor MJ, White NM. Energy harvesting vibration sources for microsystems applications. Meas Sci Technol 2006;17:R175–95.
[7] Priya S, Song H-C, Zhou Y, Varghese R, Chopra A, Kim S-G, et al. A review on piezoelectric energy harvesting: materials, methods, and circuits. Energy Harvest Syst 2017;4:1–37.
[8] Abdelmoula H, Sharpes N, Abdelkefi A, Lee H, Priya S. Low-frequency Zigzag energy harvesters operating in torsion-dominant mode. Appl Energy 2017;204:413–9.
[9] Tan Y, Dong Y, Wang X. Review of MEMS electromagnetic vibration energy harvester. J Microelectromech Syst 2017;26:1–16.
[10] Han N, Zhao D, Schluter JU, Goh ES, Zhao H, Jin X. Performance evaluation of 3D printed miniature electromagnetic energy harvesters driven by air flow. Appl Energy 2016;178:672–80.
[11] Khan FU, Qadir MU. State-of-the-art in vibration-based electrostatic energy harvesting. J Micromech Microeng 2016;26:103001.
[12] Zhang Y, Wang T, Luo A, Hu Y, Li X, Wang F. Micro electrostatic energy harvester with both broad bandwidth and high normalized power density. Appl Energy 2018;212:362–71.
[13] Deng Z, Dapino MJ. Review of magnetostrictive vibration energy harvesters. Smart Mater Struct 2017;26:103001.
[14] Naifar S, Bradai S, Viehweger C, Kanoun O. Survey of electromagnetic and magnetoelectric vibration energy harvesters for low frequency excitation. Measurement 2017;106:251–63.
[15] Wang ZL, Chen J, Lin L. Progress in triboelectric nanogenerators as a new energy technology and self-powered sensors. Energy Environ Sci 2015;8:2250–82.
[16] Rasel MSU, Park J-Y. A sandpaper assisted micro-structured polydimethylsiloxane fabrication for human skin based triboelectric energy harvesting application. Appl Energy 2017;206:150–8.
[17] Kulah H, Najafi K. Energy scavenging from low frequency vibrations by using frequency up-conversion for wireless sensor applications. IEEE Sens J 2008;8:261–8.
[18] Kimura S, Tomioka S, Iizumi S, Tsujimoto K, Sugou T, Nishioka Y, Improved performances of acoustic energy harvester fabricated using sol/gel lead zirconate titanate thin film. Jpn J Appl Phys 2011;50:06GM14.
[19] Mizuno M, Chetwynd DG. Investigation of a resonance microgenerator. J Micromech Microeng 2003;13:209–16.
[20] Wang X, Chen C, Wang N, San H, Yu Y, Halvorsen E, et al. A frequency and bandwidth tunable piezoelectric vibration energy harvester using multiple nonlinear techniques. Appl Energy 2017;190:368–75.
[21] Younesian D, Alam M-R. Multi-stable mechanisms for high-efficiency and broadband ocean wave energy harvesting. Appl Energy 2017;197:292–302.
[22] Tang L, Yang Y, Soh CK. Toward broadband vibration-based energy harvesting. J Intell Material Syst Struct 2010;21:1867–97.
[23] Ylli K, Hoffmann D, Willmann A, Becker P, Folkmer B, Manoli Y. Energy harvesting from human motion: exploiting swing and shock excitations. Smart Mater Struct 2015;24:025029.
[24] Ju S, Chae SH, Choi Y, Lee S, Lee HW, Ji C-H. A low frequency vibration energy harvester using magnetoelectric laminate composite. Smart Mater Struct 2013;22:115037.
[25] Saha CR, O'Donnell T, Wang N, McCloskey P. Electromagnetic generator for harvesting energy from human motion. Sens Actuators A 2008;147:248–53.
[26] Liu H, Gudla S, Hassani FA, Heng CH, Lian Y, Lee C. Investigation of the nonlinear electromagnetic energy harvesters from hand shaking. IEEE Sens J 2015;15:2356–64.
[27] Wei S, Hu H, He S. Modeling and experimental investigation of an impact-driven piezoelectric energy harvester from human motion. Smart Mater Struct 2013;22:105020.
[28] Halim MA, Cho H, Salauddin M, Park JY. A miniaturized electromagnetic vibration energy harvester using flux-guided magnet stacks for human-body-induced motion. Sens Actuators A 2016;249:23–31.
[29] Geisler M, Boisseau S, Perez M, Gasnier P, Willemin J, Ait-Ali I, et al. Human-motion energy harvester for autonomous body area sensors. Smart Mater Struct 2017;26:035028.
[30] Romero E, Neuman MR, Warrington RO. Rotational energy harvester for body motion. In: Proc 24th int conference on micro electro mechanical systems (MEMS); 2011. p. 1325–8.
[31] Pillatsch P, Yeatman EM, Holmes AS. A piezoelectric frequency up-converting energy harvester with rotating proof mass for human body applications. Sens Actuators A 2014;206:178–85.
[32] Nakano J, Komori K, Hattori Y, Suzuki Y. MEMS rotational electret energy harvester for human motion. J Phys Conf Ser 2015;660:012052.
[33] Lockhart R, Janphuang P, Briand D, de Rooij NF. A wearable system of micromachined piezoelectric cantilevers coupled to a rotational oscillating mass for on-body energy harvesting. In: Proc 27th int conference on micro electro mechanical systems (MEMS); 2014. p. 370–3.
[34] Yeatman EM. Energy harvesting from motion using rotating and gyroscopic proof masses. Proc Inst Mech Eng C 2008;222:27–36.
[35] Xue T, Ma X, Rahn C, Roundy S. Analysis of upper bound power output for a wrist-worn rotational energy harvester from real-world measured inputs. J Phys Conf Ser 2014;557:012090.
[36] Zhang Q, Gu L, Yang K, Halim MA, Rantz R, Roundy S. Kinetic energy harvesting using improved eccentric rotor architecture for wearable sensors. In: Proc IEEE Sensors; 2016. p. 1628–30.
[37] Rantz R, Halim MA, Xue T, Zhang Q, Gu L, Yang K, et al. Architectures for Wrist-worn Energy Harvesting. Smart Mater Struct 2018 [in press]. http://doi.org/10.1088/1361-665X/aa94d6.